Ionics (2018) 24:4081–4092
https://doi.org/10.1007/s11581-018-2727-8

SHORT COMMUNICATION

Enhanced pseudocapacitive performance of SnO_2, Zn-SnO_2, and Ag-SnO_2 nanoparticles

B. Saravanakumar[1] · S. P. Ramachandran[1] · G. Ravi[1] · V. Ganesh[2] · S. Ravichandran[3] · P. Muthu Mareeswaran[4] · R. Yuvakkumar[1]

Received: 8 February 2018 / Revised: 7 September 2018 / Accepted: 7 September 2018 / Published online: 15 September 2018

Abstract

Metal-doped tin oxide is gathering interest in the field of energy storage and power supply devices, particularly in supercapacitors applications. In the present study, we adopt a hydrothermal method to synthesis SnO_2, Zn-SnO_2, Ag-SnO_2 nanoparticles at suitable conditions of temperature, pH, reaction time, and capping agents (CTAB). SnO_2, Zn-SnO_2, Ag-SnO_2 nanoparticles were synthesized at 160 °C for 12 h and characterized by employing X-ray Diffraction to confirm the regular crystalline formation with tetragonal structure. Initial analyses by employing CV and GCD results exhibited specific capacitance of 308.2 Ag^{-1} for Ag-SnO_2 nanoparticles at current density 0.5 A/g and can be considered as suitable candidate as positive electrode for supercapacitor device applications.

Keywords Hydrothermal · CTAB · Zn-SnO_2 · Ag-SnO_2 · Supercapacitors

Introduction

Metal oxides perform a vital role in the fields such as chemistry, material science, energy science, and bio-electronics [1]. Supercapacitors have a high power density (~ 10 kW kg^{-1}), good cycle stability and fast charge and discharge speed, but their energy density is very low (~ 5 Wh kg^{-1}). While lithium-ion batteries have a high energy density (~ 150–210 Wh kg^{-1}), their power density and cycle stability are relatively poor [2]. Hence, the supercapacitor materials may consider the promising energy storage devices with quick charging and discharging capacity when their energy density is improved comparing to other storage devices such as batteries [2]. The energy storage devices like supercapacitors are utilized for quick charge/discharge cycles rather than long-term compact energy storage especially for many automotive machines, classically the combination of conductive polymers and transition metal oxides/hydroxides/sulfides/nitrides are the most excellent materials for faradic charge storage device [3–6]. The transition metal oxide (TMO)-based electrode materials such as RuO_2 [7], MnO_2 [8], NiO [9], Co_3O_4 [10], and Fe_2O_3 are extensively studied [11]. Similarly, the semiconducting materials like ZnO, SnO_2 nanomaterials have been extensively explored for large number of energy storage devices and applications. For example, nanostructured SnO_2 and its nanocomposite with different materials are used innumerous applications such as gas sensors [12–16], electrocatalytic materials [17, 18], biosensors [19], and in non-linear optics applications. Different synthesis mechanisms for oxide and various SnO_2 nanostructures have been configured for supercapacitor applications and their electrochemical properties have been studied in detail [20]. Mishra et al. have studied the LPG-sensing properties of Zn-doped and undoped SnO_2 nanoparticles, and a comparison have been made to understand the role of dopant in gas sensing applications [21]. Similarly, Zn-doped SnO_2 nanorods have been synthesized by adopting the solvothermal method and its ferromagnetic properties were investigated in detail. The study shows that the synthesized nonmagnetic Zn ion-doped SnO_2 nanorods exhibit obvious room-temperature ferromagnetism, and their saturated

✉ R. Yuvakkumar
yuvakkumar@gmail.com

[1] Nanomaterials Laboratory, Department of Physics, Alagappa University, Karaikudi, Tamil Nadu 630 003, India

[2] Electrodics and Electrocatalysis (EEC) Division, CSIR–Central Electrochemical Research Institute (CSIR–CECRI), Karaikudi, Tamil Nadu 630003, India

[3] Electro Inorganic Division, CSIR–Central Electrochemical Research Institute (CSIR–CECRI), Karaikudi, Tamil Nadu 630003, India

[4] Department of Industrial Chemistry, Alagappa University, Karaikudi, Tamil Nadu 630003, India

magnetic moment is sensitive to the concentration of Zn dopant. Based on d^0 ferromagnetism, the observed ferromagnetic ordering of $Sn_{1-x}Zn_xO_2$ nanorods could be related to the doping-induced V_{Sn} defects [22]. Mohamed Rashad and his collaborators describe the decomposition of methylene blue on transition metal-doped SnO_2 nanoparticles and the detailed studies explained the following points clearly that Zn^{2+}-doped SnO_2 ($Zn_{0.3}Sn_{0.7}O_2$) was remarked the highest photo catalytic activity for the MB photo degradation. The improvement in the photo catalytic activity of $Zn_{0.3}Sn_{0.7}O_2$ is endorsed to heterojunctions of ZnO/SnO_2. The effect of doping Ni, Co, and Mn ions on the photo catalytic properties are insignificant in the photo catalytic activity of SnO_2. The recycling tests indicated that ZnO/SnO_2 was quite stable and there is no decrease in photo catalytic activity after five-time repetition, indicating a promising catalyst for commercial applications [23]. Vignesh and his group demonstrated the photo catalytic performance of Ag-doped SnO_2 nanoparticles modified with curcumin in their work. The photocatalytic activity was measured by the degradation of rose Bengal and Ag and curcumin modification enhanced the photocatalytic activity of SnO_2. In the same way, Cur–Ag–SnO_2 is also showed antifungal activity against *Candida alb cans* [24]. Another work on thermoluminescence response and dose-linearity of SnO_2 nanoparticles have been improved on 1.0% Ag doping, and subsequent thermal annealing. However, a higher Ag content causes the formation of Ag clusters, reducing both the thermoluminescence and photo luminescence responses of the nanoparticles [25]. In addition, Kumar and his co-workers adopted the dip-coating method to prepare ceria electrode material made by uniform doping of silver and platinum nanoparticles for high performance supercapacitors applications [26]. The silver doping revealed 1017 Fg^{-1} specific capacitance at 1 Ag^{-1} current density, a fivefold increase, while platinum doping revealed a tenfold increase in specific capacitance, i.e., 1987 Fg^{-1} at 1 Ag^{-1} current density [26]. Similarly, the doping of nickel and graphite can increase the electrical conductivity and the specific surface area of nano-amorphous TiO_2 [27]. The initial capacity of the composite electrode material TiO_2-NiO-C was 13.4 mAh/g, and the value dropped slightly to 12.88 mAh/g after 500 cycles [27]. Moreover, Tung and his co-workers explored the electrode position method to synthesis Fe- and Co-doped manganese oxides composed of nanofiber-like structure with 5–20 nm radius and studied its electrochemical properties [28]. The specific capacitance value of deposited manganese oxide reaches a maximum of 175.3 F/g for Co doping and 244.6 F/g for Fe doping. The obtained thin films retained about 84% of the initial capacity even after 500 cycles of charge–discharge test [28]. Dong and

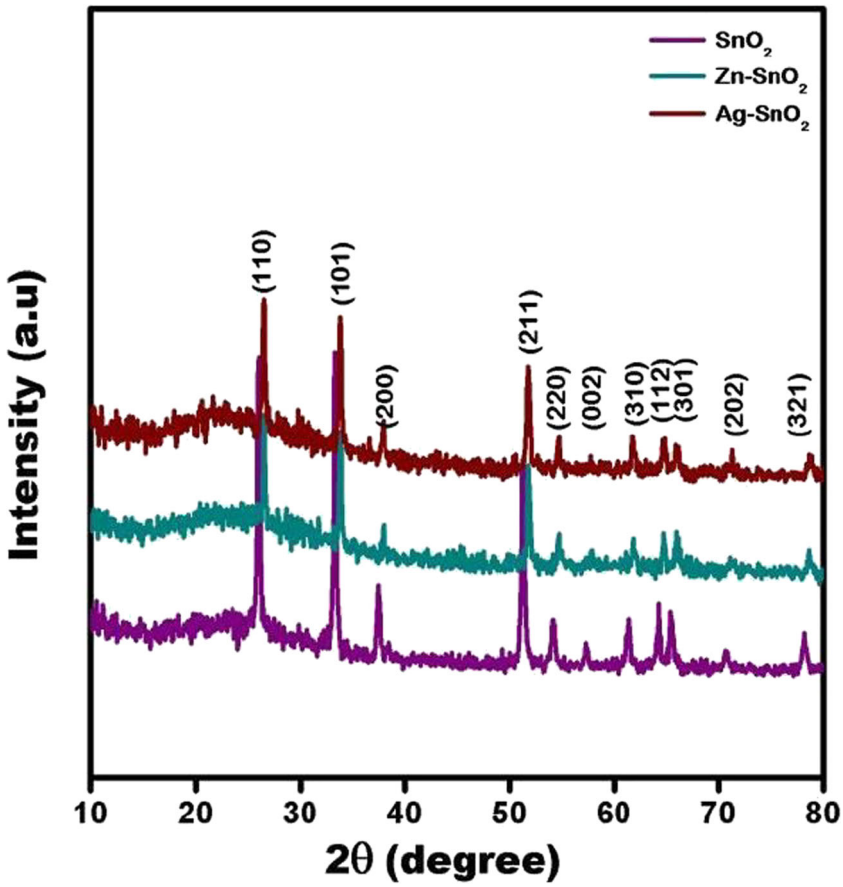

Fig. 1 XRD pattern **a** SnO_2, **b** Zn-SnO_2, **c** Ag-SnO_2 nanoparticles

his co-workers discussed clearly about enhanced supercapacitors performance of Mn_3O_4 nanocrystals by doping transition-metal ions and evaluated the specific capacitance of Cr-doped Mn_3O_4 nanocrystals which exhibits 272 F g^{-1} at a current density of 0.5 A g^{-1} [29].

Even though SnO_2-based materials have been used for several related applications in wide spectrum of area, the study on the effect of transition metal doping (Zn and Ag) on SnO_2 nanoparticles for different electrochemical supercapacitors applications was rarely studied. Hence, in the present study, we try to understand and establish the impact of Zn and Ag dopants on the SnO_2 nanoparticles as electrode for supercapacitor applications. Further, the role of high conductive silver (Ag) dopant and low electrical conductive zinc (Zn) dopant on the SnO_2 nanoparticles will be investigated based on their electrochemical properties for pseudocapacitive electrode applications. Hence, in the present study, SnO_2, Zn-SnO_2, Ag-SnO_2 nanostructures have been successfully synthesized and investigated its electrochemical properties as pseudocapacitive electrode applications.

Experimental methods

In this work, we implement hydrothermal synthesis procedure to obtain SnO_2 nanoparticles with different molar concentration of precursor. 0.758 g tin chloride ($SnCl_2$) salt is mixed with ethanol. The dissolved precursor slats in a beaker were stirred for 30 min to attain homogeneity of solution. Five millimolars CTAB as surfactant was added to the above solution. The homogenous precursor solution was transferred to 100 ml teflon-coated autoclave and maintained at 160 °C for 12 h. Then, the autoclave is allowed to cool down to room temperature naturally. The obtained powder were cleaned and washed by distilled water and ethanol for three times to remove the untreated salts precursors and impurities. Then, the cleaned products were dried in hot air oven at 80 °C for overnight and named as SF1. The same procedure was followed for other two products by introducing the metal dopant of 2 mM $ZnCl_2$ solution added with tin chloride solution precursor and the final product was named as SJ1. Similarly, 2 mM $AgCl_2$ solution was added with tin chloride solution precursor and final product was named as SK1. The electrochemical properties of obtained product were

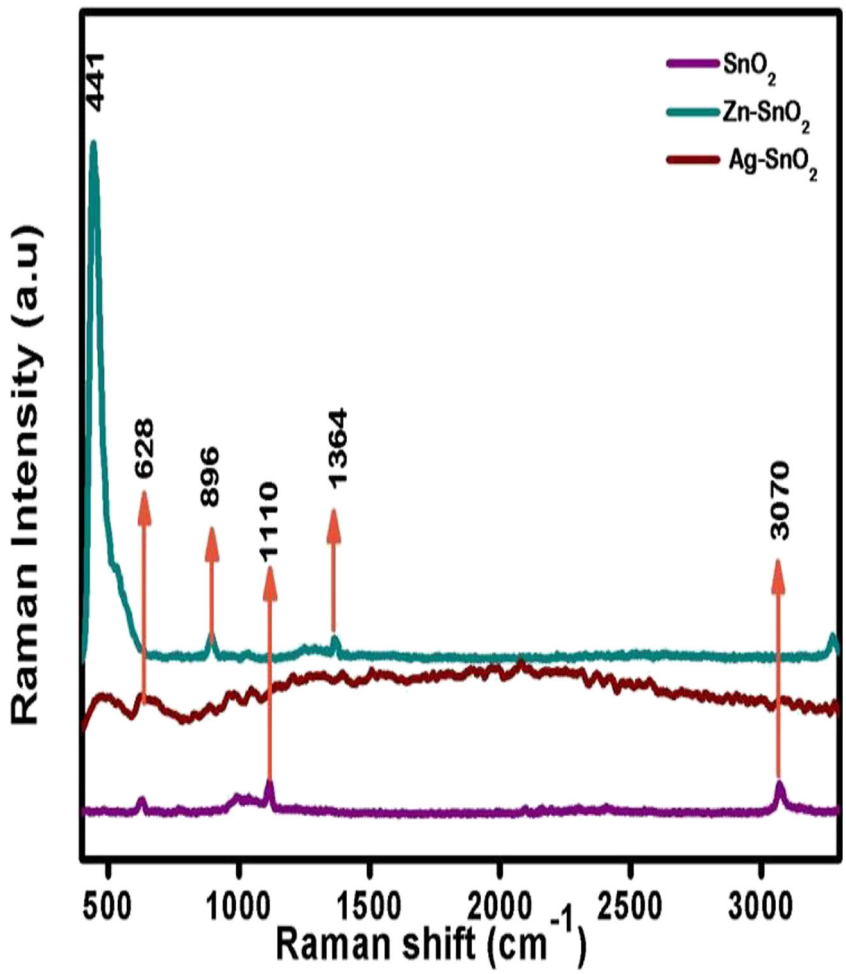

Fig. 2 Raman spectra **a** SnO_2, **b** Zn-SnO_2, **c** Ag-SnO_2 nanoparticles

analyzed by employing CH660D instrument with three electrode cell configuration. Ag/AgCl, platinum wire and SnO_2, Ag-SnO_2 and Zn-SnO_2 coated on Ni-foam were acted as references, counter and working electrodes respectively. The working electrode was prepared by dissolving Ni-Foam in 3 M of HCl for 30 min under sonication to remove the oxide layer in Ni-foam. After that the slurry was prepared by taking active material, activated carbon (AC) and Polyvinylidene fluoride (PVDF) in the ratio of 80:15:5 with N-methly2-pyyrolidone (NMP) as solvent. The mass of active material loaded on the Ni-foam can be estimated by measuring the weight of the Ni-foam before and after coating the active materials. In this work, the measured mass of active materials was about 2 mg. The slurry was coated on to the Ni-foam of area 1 cm × 1 cm and dried at 80 °C in a hot air oven for 12 h.

Results and discussion

The X-ray diffraction method is adopted to understand the crystallinity of obtained nanoparticles. Figure 1a, b, c reveals the crystalline structure formation of synthesized SnO_2, Zn-SnO_2, and Ag-SnO_2 nanoparticles. The observed peaks at 26°, 33.3°, 37.4°, 51.2°, 54.2°, 57.3°, 61.4°, 64.3°, 65.4°, 70.7°, and 78.1° can be associated with (110), (101), (200), (211), (220), (002), (310), (112), (301), (202), and (321) planes matched with JCPDS No:88-0287. The synthesized SnO_2 nanoparticles encompass the tetragonal crystal structure belongs to $P4_2/mnm$ (136) space group with lattice parameter $a = 4.737$, $c = 3.186$, volume of unit cell = 71.51. The observed XRD pattern for Zn-SnO_2 and Ag-SnO_2 shows a slight shift from SnO_2 which inhibits the incorporation of dopant ions (Zn and Ag) onto the lattice of SnO_2 nanoparticles. The decrease in intensity and shift in the diffraction peak probably may due to the dopant effect of Zn^{2+} and Ag^{2+} ions on to the lattice of tetragonal crystal structure of SnO_2 nanoparticles [30–32]. The Scherer formula for determination of crystalline size was used as follows, $\boldsymbol{Dp} = \frac{0.94*\lambda}{\beta Cos\theta}$, where $\boldsymbol{Dp}$ is the crystallite size, λ the wavelength of the X-ray, β1 the wavelength of full width half maximum, and θ the diffraction angle [33–39]. The evidently distinctive peaks suggesting the formation of high-quality crystalline structure with average crystalline size of sample SF1, SJ1, and SK1 as 36.63 nm, 44.39 nm, and 36.63 nm.

The obtained Raman spectra for the obtained products (SF1, SJ1, SK1) exhibited the similar peaks at 441, 628, and

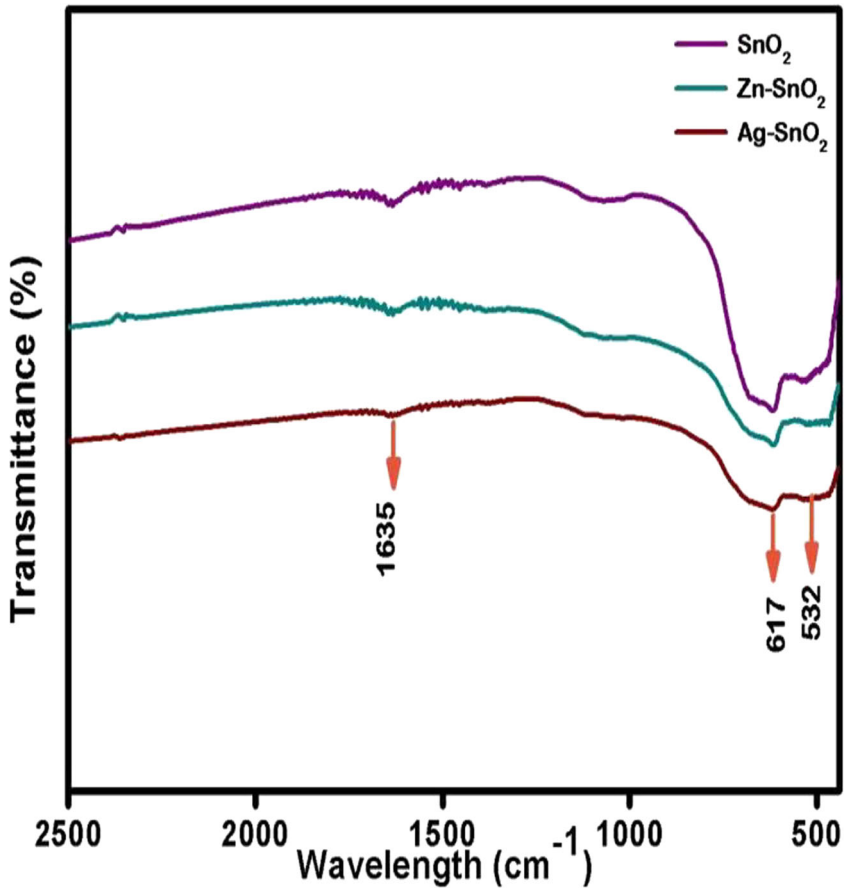

Fig. 3 IR spectra **a** SnO_2, **b** Zn-SnO_2, **c** Ag-SnO_2 nanoparticles

896 cm^{-1} which corresponds to the vibrations of Sn–O modes (Fig. 2a, b, c). The observed extra peak at 441 cm^{-1} exhibited for SJ1 can be attributed to the Zn–O vibration modes and predicts the dopant Zn^{2+} ions exactly placed on the lattice planes of SnO_2 nanoparticles. Correspondingly, the appearance of board peak around the 475 cm^{-1} may be the contribution of metal oxide bond vibration due to the dopant role of Ag^{2+} ions and was exactly placed on the lattice plane of SnO_2 nanoparticles. The peak observed at 628 and 896 cm^{-1} can be attributed to the vibration modes of O–Sn–O, especially 628 cm^{-1} corresponds to A_{1g} modes of Sn–O vibrations and peak at 896 can be attributed to the B_{2g} vibration modes of Sn–O [40–42]. The other small peaks at 1110 and 1364 cm^{-1} may be corresponds to the secondary Raman peaks for SnO_2 nanoparticles.

The vibrational properties of constituent metal oxides and the functional groups present in the synthesized nanomaterials can be investigated by performing InfraRed analysis (FTIR). We have performed Mid-FTIR studies typically range from 400 to 4000 cm^{-1}. This range can be classified into two regions: 400–1000 cm^{-1} as finger print region and 1000–4000 cm^{-1} as functional group region. In Fig. 3a, b, c, for all obtained products SF1, SJ1, and SK1, the peaks appeared at 532 and 617 cm^{-1} falls on the finger print region corresponds to the vibration mode of LO phonon due to $E\|$ to the C-axis [43] and the antisymmetric vibration of Sn–O–Sn mode corresponding to E_u vibration modes of TO phonon [44–46] respectively. A small peak observed at 1630 can be readily indexed to the C–O and C=O vibration modes [47].

The SEM micrograph shows the nanoparticles formation of all the three products as shown in the Fig. 4a, b, c. Nevertheless, the experimental parameter conditions are same for all products expect the addition of dopant, the results seem similar in the formation of nanoparticles; it is evident from the Fig. 4a, b, c. All obtained products SF1, SJ1, and SK1 have same uniform distribution of the spherical nanoparticles synthesized at the optimized experimental conditions. The EDS studies displayed in Fig. 5a, b, c confirms the addition of dopant Zn^{2+} and Ag^{2+} ions on to the SnO_2 nanoparticles. The uniform formation of nanoparticles is facilitating from the CTAB surfactant role in the nucleation mechanism formation which can be rightly evidenced from the SEM micrographs.

To understand the electrochemical behavior of the synthesized products cyclic voltammetry (CV), galvanostatic charging–discharging (GCD) studies has been performed to evaluate

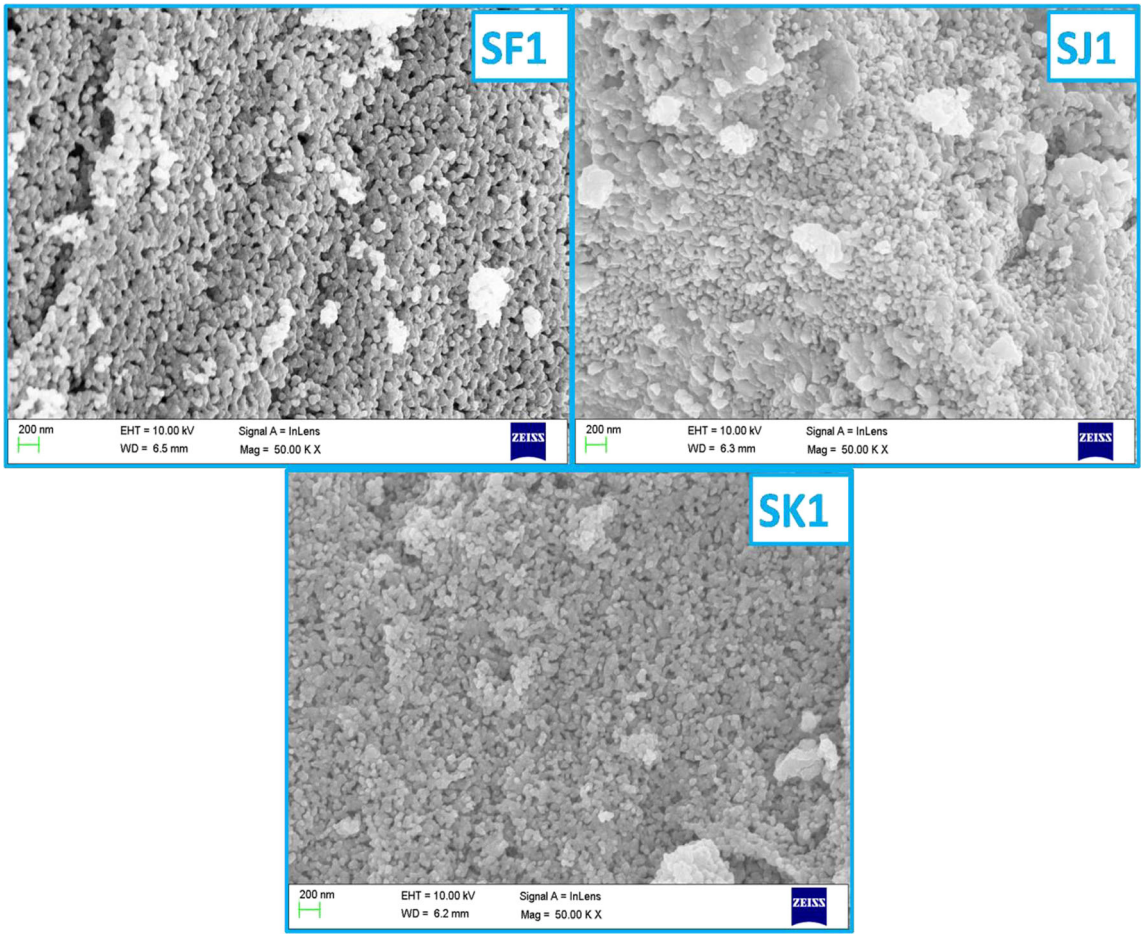

Fig. 4 SEM images **a** SnO_2, **b** Zn-SnO_2, **c** Ag-SnO_2 nanoparticles [200 nm scale]

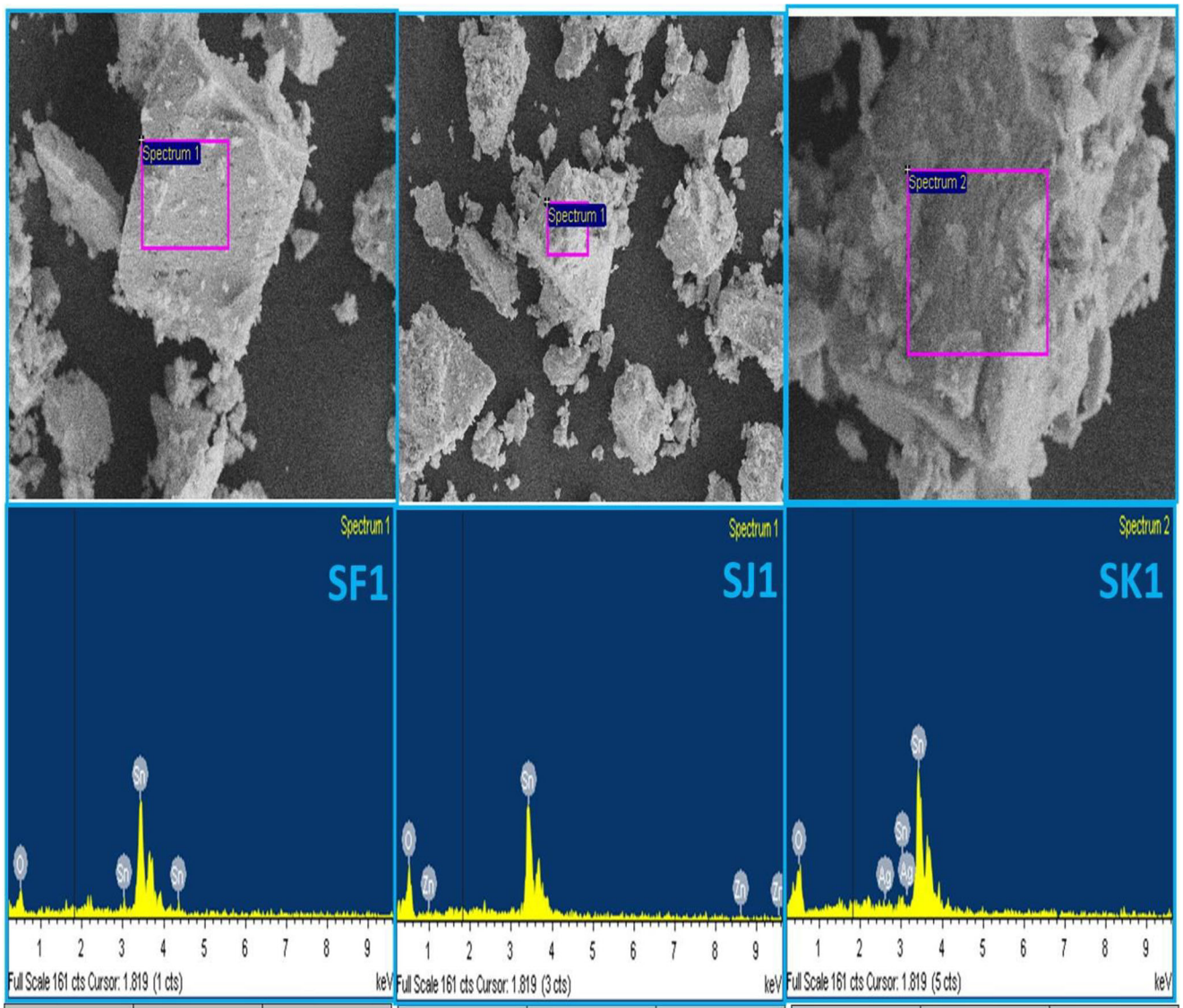

Element	Weight %	Atomic%
O K	24.12	70.23
Sn L	75.88	29.77

Element	Weight %	Atomic%
O K	32.59	77.14
Zn K	5.20	3.01
Sn L	62.21	19.85

Element	Weight %	Atomic%
O K	31.47	77.23
Ag L	2.83	1.03
Sn L	65.70	21.74

Fig. 5 EDS spectra **a** SnO_2, **b** Zn-SnO_2, **c** Ag-SnO_2 nanoparticles

the capacitance abilities. Figure 6a, b, c shows the cyclic voltammetry curves for SF1, SJ1, and SK1 having similar curves pattern with redox peaks, one in positive potential and another in the negative region of potential window 0–0.6 V. The CV curve for pure SnO_2 (SF1) exhibits smaller curve area with uniform increase in the oxidation and reduction voltage as the scan rate increases. Similarly, the shift in the redox peaks are also observed in both the positive and negative region due to the

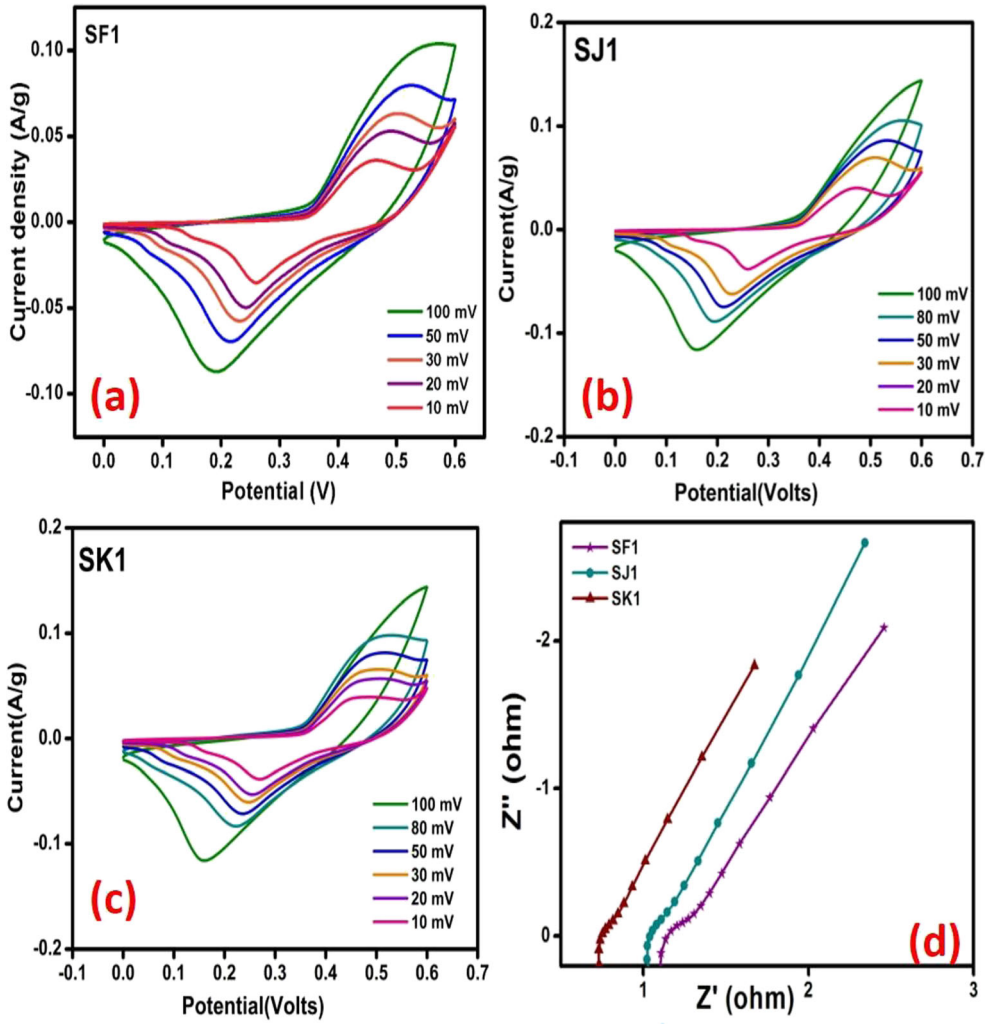

Fig. 6 SnO_2 nanoparticles **a**–**c** CV curve for SF1, SJ1, and SK1 at different scan rates **d** EIS spectra for SF1, SJ1, and SK1

fact that, the high scan rate results the less time to interact OH^- with the active material of the working electrode. The same pattern can also be evidenced in all the CV curves of the obtained products. The different scan rate is adopted for the CV studies as 10, 20, 30, 50, 80, 100 mV/s and its corresponding specific capacitance can be estimated from the following expression $\boldsymbol{C} = \int \frac{\boldsymbol{IdV}}{\boldsymbol{ms}\ (\boldsymbol{V2}-\boldsymbol{V1})}$, where C is the specific capacitance of active material, IdV the integral sweep area by CV curve, m the mass of the active material coated on Ni-foam, s the scan rate, and $(V2 - V1)$ the applied potential window of electrolyte. The estimated specific capacitances for all the obtained products (SF1, SJ1, SK1) are tabulated in Table 1. The calculated specific capacitance value reveals that the dopant zinc ions (Zn) and silver ions (Ag) plays a significant role in the capacitance ability of the SnO_2 nanoparticles. The role of different dopant Zn^{2+}- and Ag^{2+}-doped onto the lattice of the SnO_2 nanoparticles could be easily revealed form the specific capacitance values. The observed results shows that the metal dopant Ag^{2+} on SnO_2 (Ag-SnO_2) gives rise to high conductivity than the semiconductor dopant Zn^{2+} on SnO_2 (Zn-SnO_2). Though the variation in specific capacitance seems small for the different dopant, the role of the active sites in the working electrode with corresponding dopant has been the cause for capacitive performances.

Table 1 Specific capacitance of synthesized SnO_2 nanoparticles (SF1, SJ1, and SK1) at different scan rates

Potential (V)	Scan rate (mV/s)	Specific capacitance (F/g)		
		SF1	SJ1	SK1
0.6	10	576.1	645.1	718.6
0.6	20	460.3	525.3	585.6
0.6	30	378.9	389.9	407.0
0.6	50	292.2	302.2	327.3
0.6	100	186.9	204.9	246.8

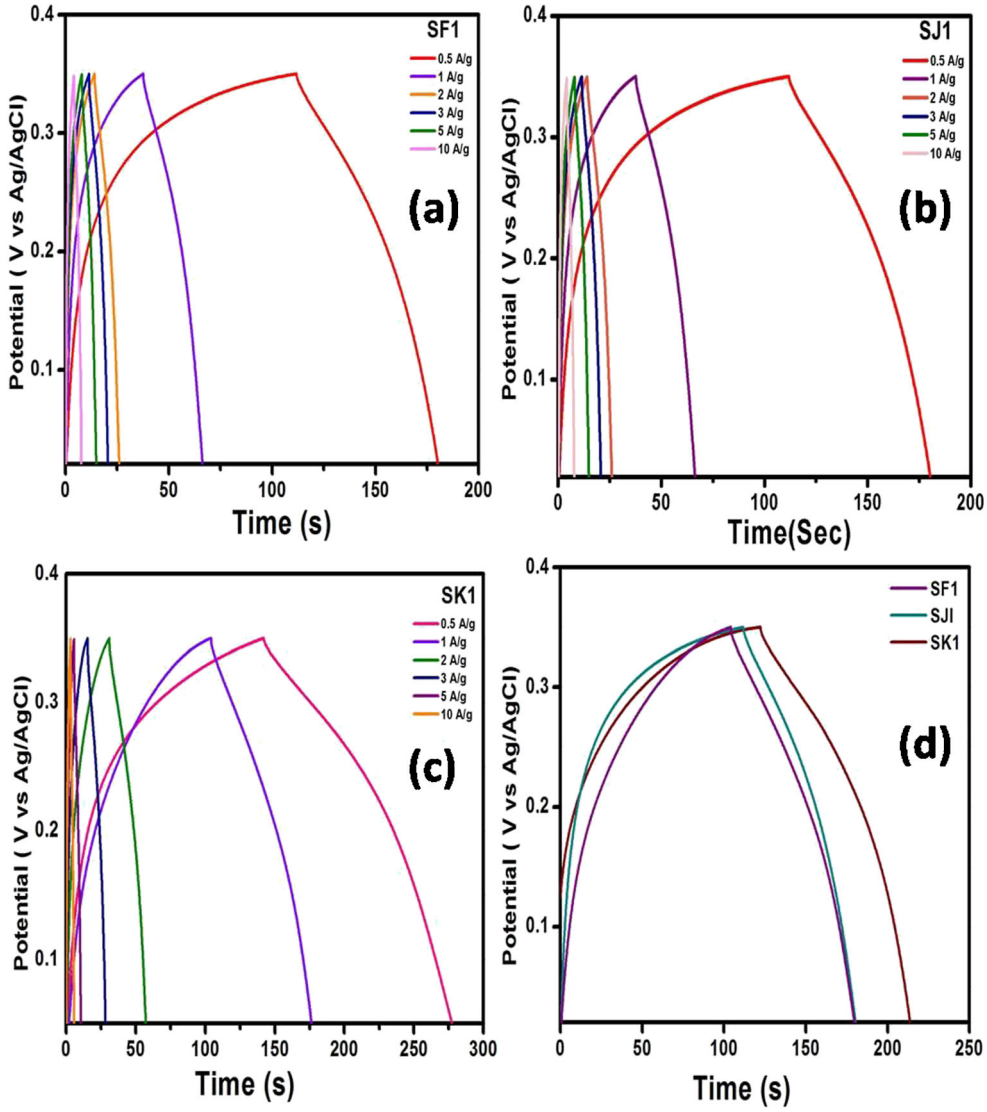

Fig. 7 GCD studies of SnO_2 nanoparticles **a**–**c** CV curve for SF1, SJ1, SK1 at different current density **d** comparative GCD curve for SF1, SJ1, and SK1 at 0.5 A/g

In order to evaluate the capacitive behavior in a detailed manner, generally electroimpedance analysis have been instituted and its character is estimated for all obtained products for the AC frequency range 10 mHz−100 kHz. Figure 6d reveals the EIS spectra for all three SnO_2, Zn-SnO_2, and Ag-SnO_2 nanoparticles and the high conductivity for the Ag-SnO_2 nanoparticles can be explained in the terms of the presence of metal ions in the place of SnO_2 lattice enhances its capacitive nature. The contact resistance (R_{ct}) arises from the electrode and electrolyte interaction and the solution resistance (R_s) at high frequency of applied AC field has been investigated from the Fig. 6d. The measured R_{ct} values such as 1.23 Ω, 1.06 Ω, and 0.61 Ω for SnO_2 (SF1), Zn-SnO_2 (SJ1), and Ag-SnO_2 (SK1) nanoparticles indicates that SK1 have demonstrated the low contact resistance when compared to SJ1 and SF1 along with a small semi-arc with high spike overtone and revealed the good capacitive nature which reflects in the specific capacitance values. At low frequency range, the Warburg resistance also seems similar trend, in

Table 2 Specific capacitance of synthesized SnO_2 nanoparticles (SF1, SJ1, and SK1) at different current density

Potential (V)	Current density (A/g)	Specific capacitance (F/g)		
		SF1	SJ1	SK1
0.35	0.5	257.1	274.8	308.2
0.35	1	221.7	259	278.2
0.35	2	161.4	221.4	246.4
0.35	3	143.3	208.5	224.7
0.35	5	110.9	176.1	199.4
0.35	10	77.1	94.4	155.3

Table 3 The comparison of SnO_2 by different literature on storage device applications

Materials	Cell configuration	Specific capacitance (F/g)	Current density	References
SnO_2 thin films	Three-electrode cell system	66 Fg^{-1}	10 mV/s	R5
Hierarchical SnO_2	Three-electrode cell system	187.7 Fg^{-1}	1.0 A g^{-1}	R6
Polyaniline/SnO_2	Three-electrode system	305.3 F g^{-1}	0.5 A g^{-1}	R7
Ni/SnO_2 nanoflowers	Three-electrode system	410 mF cm^{-2}	1 $mAcm^{-2}$	R8
Ag-SnO_2	Three-electrode system	308.2 Ag^{-1}	0.5 A g^{-1}	This work

which the SK1 have greater slope than the SJ1 and SF1 which can help to achieve high capacitance.

In addition, the galvanostatic charging and discharging studies have been employed for all three SnO_2, Zn-SnO_2, and Ag-SnO_2 nanoparticles to understand its charging capacity. Fig. 7a, b, c, d shows the GCD studies with symmetry curves and explains the good capacitive nature without any IR drop in the discharging region. This feature enables the SnO_2, Zn-SnO_2, and Ag-SnO_2 nanoparticles as suitable candidate for positive electrode for supercapacitor applications. For comparison, the GCD curves for all products at current density 0.5 A/g is displayed in Fig. 7d. Ag-SnO_2 nanoparticles perform well with superior specific capacitance. The specific capacitance of the all products is measured by adopting the following equation $Cs=\frac{I\nabla t}{m\nabla V}$, where I is the current applied to cathode, ∇t the discharging time, m the mass of the active material, and ∇V the potential window [48]. The evaluated specific capacitance for SnO_2, Zn-SnO_2, and Ag-SnO_2 nanoparticles for different current densities 0.5, 1, 2, 3, 5, and 10 A/g are tabulated in Table 2. It explains the same pattern as cyclic voltammetry studies that, the Ag-SnO_2 nanoparticles exhibit the superior specific capacitance presumably due to the presence of metal ions in lattice of tin oxide which enables the access to more active sites than the tin oxide nanoparticles. Moreover, the observed FESEM images of the obtained product clearly revealed that all the three products (SF1, SJ1, SK1)

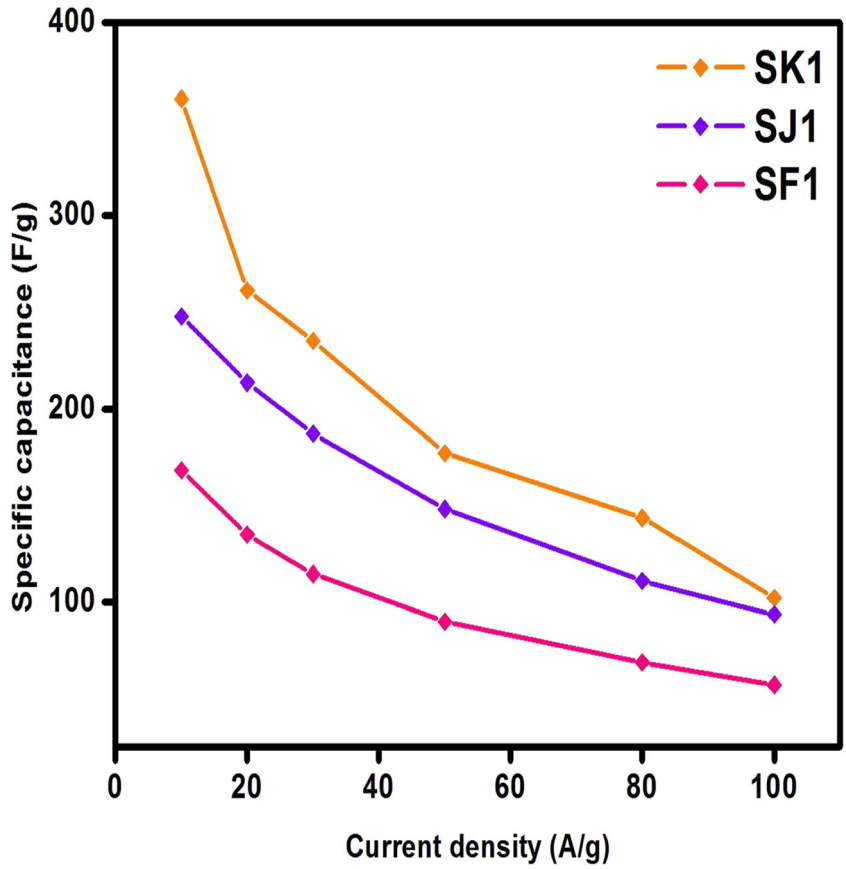

Fig. 8 Specific capacitance Vs Current density **a** SnO_2, **b** Zn-SnO_2, **c** Ag-SnO_2

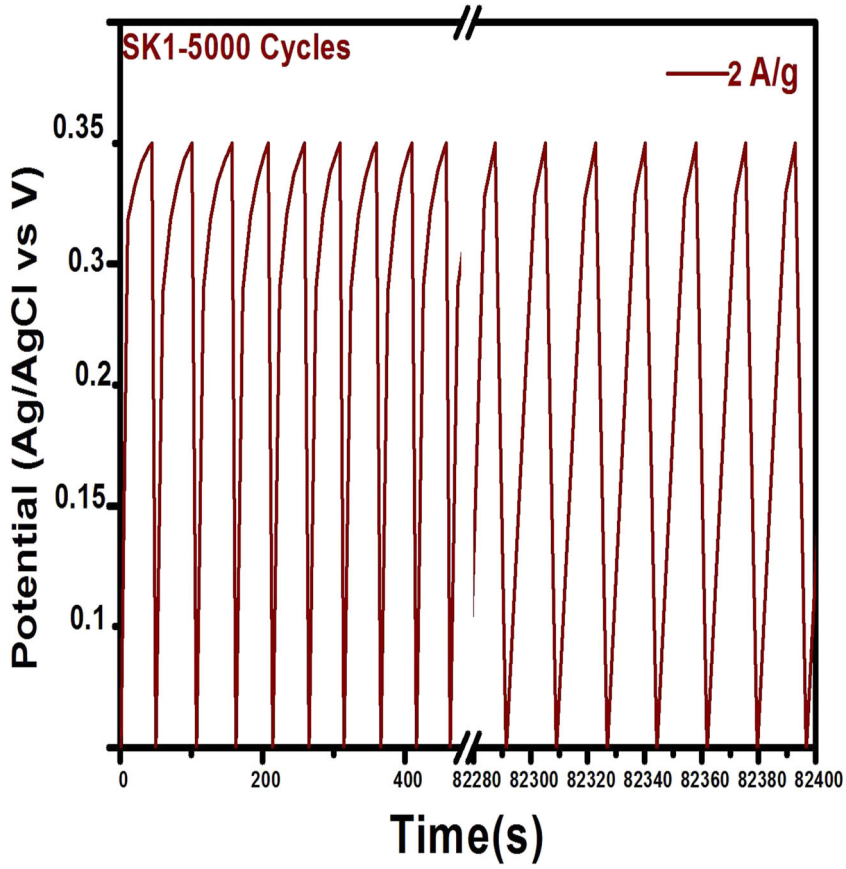

Fig. 9 Cyclic stability GCD curve of Ag-SnO_2 for 5000 cycles at current density of 2 A/g

possess same uniform spherical nanoparticles since synthesized at same experimental procedure and conditions. Hence, the variation or an increase in the specific capacitance of Ag-SnO_2 was mainly contributed from the dopant Ag^{2+} and that can be supported by many reports [29, 49]. In charging and discharging profile, all three obtained products have been limited to 0.35 V due to the potential window limitation of synthesized materials. In the CV test, the electrode potential window is 0.6 V, but in GCD measurement, the potential window is reduced to 0.35 V. It is due to fact that in CV studies the different ranges of potential window have been explored for obtaining information on redox reaction process and finally 0–0.6 V window is demonstrated. In GCD studies, initially 0–0.5 V potential window has been explored for SnO_2 nanoparticles. However, at low current density (0.5 A/g and 1 A/g), symmetrical GCD curve has not been achieved with low columbic efficiency in charging and discharging process. In order to execute and reveal its symmetrical and high columbic efficiency, the optimized potential window for SnO_2 nanoparticles has been opted as 0–0.35 V. Further, as the current density increased as 1, 2, 3, 5, and 10 Ag^{-1}, the GCD curves displays very good symmetrical charging and discharging pattern which results in the good coulomb efficiency of all three obtained products.

The calculated specific capacitance of the synthesized Ag-SnO_2 (SK1) nanoparticles can be compared with already reported results as shown in Table 3. Pusawale et al. has adopted an expensive chemical route to synthesis nanocrystalline SnO_2 thin films and tested for supercapacitor applications. The observed results revealed the specific capacitance of 66 Fg^{-1} in 0.5 Na_2SO_4 electrolytes at 10 mVs^{-1} scan rate [50]. Liu et al. also demonstrated the hierarchical SnO_2 nanostructures synthesized by employing facile hydrothermal process and its electrochemical studies reveals 187.7 Fg^{-1} specific capacitance at 1 Ag^{-1} current density and also can be efficiently used as photo catalyst, gas sensing materials [51]. Polyaniline/SnO_2 nanocomposite exhibits the superior specific capacitance of 305.3 Fg^{-1} with a specific energy density of 42.4 Wh kg^{-1} and a coulombic efficiency of 96%. These results explain the synergistic effect of PANI/SnO_2 which complements the properties of both materials [52]. The Ni/SnO_2 nanoflowers exhibited enhanced capacitance of 410 mF cm^{-2} at discharge currents of 1 $mAcm^{-2}$ and capacity retention keeping 91% when the discharge current density increased from 1 $mAcm^{-2}$ to 10 $mAcm^{-2}$ [53]. Moreover, the effective interaction between the metal ions (Ag^{2+}) in the working electrode with OH^- ions from electrolyte and quick kinetics of the OH^- ions in the form of intercalation and deintercalation

between active sites enables the superior capacitive characteristics of the Ag-SnO_2 nanoparticles [54, 55]. The reason behind the superior capacitive nature might be the uniform distribution of Ag-SnO_2 nanoparticles with uniform spherical nanoparticles configuration which enables more number of the active sites due to the presence of Ag^{2+} ions and hence initiates the faradic kinetics in the electrolyte (Fig. 8).

To understand the solidity of the pseudocapacitive materials, the cyclic stability test has been investigated in order to acquire an insight into the performance of nanomaterials for large number of galvanostatic charging and discharging cycles. Figure 9 depicts the GCD cyclic stability of SK1 at a current density of 2 Ag^{-1} for 5000 cycles. The GCD stability curves explored that the first and last few cycles of the stability test clearly reveals the superior materials permanence for large GCD cycles; especially SK1 maintains the 67% specific capacitance after 5000 cycles at current density 2 Ag^{-1}. Owing to the superior cyclic stability, Ag-SnO_2 can be considered as an efficient electrode for pseudo capacitance applications in near future. The specific capacitance 308.2 Ag^{-1} of Ag-SnO_2 nanoparticles at current density 0.5 A/g withstand for higher current density and will guaranteed as an appropriate positive electrode for supercapacitor device applications.

Conclusions

In this work, we have adopted hydrothermal method to synthesis SnO_2, Zn-SnO_2, Ag-SnO_2 nanoparticles at suitable conditions of temperature, pH, and reaction time with CTAB as capping agents. Ag-SnO_2 nanoparticles synthesized at 160 °C for 12 h exhibited better electrochemical performance. The presence of dopant (Ag, Zn) and morphology of synthesized Zn-SnO_2 and Ag-SnO_2 nanoparticles was examined by FESEM-EDS analysis and revealed the uniform spherical configuration of all three obtained nanoparticles. The synthesized Ag-SnO_2 (SK1) nanoparticles in uniform spherical nanoparticles configuration enables large number of the active sites due to the presence of Ag^{2+} ions which initiates the faradic kinetics in electrolyte. The specific capacitance 308.2 Ag^{-1} of Ag-SnO_2 nanoparticles at current density 0.5 A/g can be considered as suitable candidate as positive electrode for supercapacitor device applications.

Funding information This work was supported by UGC Start-Up Research Grant No. F.30-326/2016 (BSR).

References

1. Conway BE (1999) Electrochemical supercapacitors: scientific fundamentals and technological applications. Springer, New York
2. Wang G, Zhang L, Zhang J (2012) A review of electrode materials for electrochemical supercapacitors. Chem Soc Rev 41:797–828
3. Simon P, Gogotsi Y (2008) Materials for electrochemical capacitors. Nat Mater 7:845–854
4. Bao SJ, Li CM, Guo CX, Qiao Y (2008) Biomolecule-assisted synthesis of cobalt sulfide nanowires for application in supercapacitors. J Power Sources 180:676–681
5. Lokhandea CD, Dubala DP, Joo OS (2011) Metal oxide thin film based supercapacitors. Curr Appl Phys 11:255–270
6. Gupta V, Gupta S, Miura N (2008) Potentiostatically deposited nanostructured Co_xNi_{1-x} layered double hydroxides as electrode materials for redox-supercapacitors. J Power Sources 175:680–685
7. Liu T, Pell WG, Conway BE (1997) Self-discharge and potential recovery phenomena at thermally and electrochemically prepared RuO_2 supercapacitor electrodes. Electrochim Acta 42:3541–3552
8. Wang P, Zhao YJ, Wen LX, Chen JF, Lei ZG (2014) Ultrasound–microwave-assisted synthesis of MnO_2 supercapacitor electrode materials. Ind Eng Chem Res 53:20116–20123
9. Xia XH, Tu JP, Mai YJ, Wang XL, Gu CD, Zhao XB (2011) Self-supported hydrothermal synthesized hollow Co_3O_4 nanowire arrays with high supercapacitor capacitance. J Mater Chem 21:9319–9325
10. Shivakumara S, Penki TR, Munichandraiah N (2014) Preparation and electrochemical performance of porous hematite (α-Fe_2O_3) nanostructures as supercapacitor electrode material. J Solid State Electrochem 18:1057–1066
11. Kim SI, Lee JS, Ahn HJ, Song HK, Jang JH (2013) Facile route to an efficient NiO supercapacitor with three-dimensional nanonetwork morphology. ACS Appl Mater Interfaces 5:1596–1603
12. Bhardwaj N, Mohapatra S (2016) Structural, optical and gas sensing properties of Ag-SnO_2 plasmonic nanocomposite thin films. Ceram Int 42:17237–17242
13. Ge S, Zheng H, Sun Y, Jin Z, Shan J, Wang C, Wu H, li M, Meng F (2016) Ag/SnO_2/graphene ternary nanocomposites and their sensing properties to volatile organic compounds. J Alloys Compd 659: 127–131
14. Wei F, Zhang H, Nguyen M, Ying M, Gao R, Jiao Z (2015) Template-free synthesis of flower-like SnO_2 hierarchical nanostructures with improved gas sensing performance. Sensors Actuators B Chem 215:15–23
15. Lia M, Zhu H, Wang B, Cheng J, Yana W, Xiaa S, Tang Z (2016) Ultrasensitive and highly selective detection of methoxy propanol based on Ag-decorated SnO_2 hollow nanospheres. Sensors Actuators B Chem 232(545–556
16. Rakibuddin MD, Ananthakrishnan R (2016) Novel Ag deposited nano coordination polymers derived porous SnO_2/NiO hetero nanostructure for enhanced photo catalyticreduction of Cr(VI) under visible light. New J Chem 40:385–3394
17. Dong B, Hu WH, Zhang XY, Wang J, Lu SS, Li X, Shang X, Liu YR, Han GQ, Chai YM, Liu CG (2017) Facile synthesis of hollow SnO_2 nanospheres uniformly coated by Ag for electro-oxidation of hydrazine. Mater Lett 189:9–12
18. Hassan MAM, Hateef AA, Majeed AMA, Al-Jabiry AJM, Jameel S, Abdul Hussian HAR (2014) Amperometric biosensor of SnO_2 thin film modified by Pd, In and Ag nanostructure synthesized by CSP method. Appl Nanosci 4:927–934
19. Ghanaatshoar M, Moradi M, Tohidi P (2014) Surface Plasmon resonance enhancement of the magneto-optical Kerr effect in Cu/Co/Ag/SnO_2 structure. Eur Phys J Appl Phys 68:10402–10406
20. Gupta A, Dhakate SR, Gurunathan P, Ramesha K (2017) High rate capability and cyclic stability of hierarchically porous Tin oxide (IV)–carbon nanofibers as anode in lithium ion batteries. Appl Nanosci 7:449–462
21. Mishra RK, Sahay PP (2012) Zn-doped and undoped SnO_2 nanoparticles: a comparative structural, optical and LPG sensing properties study. Mater Res Bull 47:4112–4118
22. Liu X, Iqbal J, Wu Z, He B, Yu R (2010) Structure and room-temperature ferromagnetism of Zn-doped SnO_2 nanorods prepared by solvothermal method. J Phys Chem C 114:4790–4796

23. Rashad MM, Ismail AA, Osama I, Ibrahim IA, Kandil AHT (2014) Decomposition of methylene blue on transition metals doped SnO_2 nanoparticles. Clean: Soil, Air, Water 42:657–663
24. Vignesh K, Hariharan R, Rajarajan M, Suganthi A (2013) Photocatalytic performance of Ag doped SnO_2 nanoparticles modified with curcumin. Solid State Sci 21:91–99
25. Sánchez Zeferino R, Pal U, Meléndrez R, Barboza Flores M (2013) PL and TL behaviors of Ag-doped SnO2 nanoparticles: effects of thermal annealing and Ag concentration. Advances in Nano Research 1:193–202
26. Kumar R, Agrawal A, Nagarale RK, Sharma A (2016) High performance supercapacitors from novel metal-doped ceria-decorated aminated graphene. J Phys Chem C 120:3107–3116
27. Hong W, Zhiyuan T, Lei S, Yanbing H, Yaxiana W, Zhongyan L (2009) Capacitance performance enhancement of TiO_2 doped with Ni and graphite. Rare Metals 28:231–236
28. Tung MT, Thuy HTB, Hang LTT (2015) Metal doped manganese oxide thin films for supercapacitor application. J Nanosci Nanotechnol 15:6949–6956
29. Dong R, Ye Q, Kuang L, Lu X, Zhang Y, Zhang X, Tan G, Wen Y, Wang F (2013) Enhanced supercapacitor performance of Mn_3O_4 nanocrystals by doping transition-metal ions. ACS Appl Mater Interfaces 5:9508–9516
30. Kumar S, Sahare PD (2014) Gd^{3+} incorporated ZnO nanoparticles: a versatile material. Mater Res Bull 51:217–223
31. Lerner I, Trus M, Cohen R, Yizhar O, Nussinovitch I, Atlas D (2006) Ion interaction at the pore of Lc-type Ca^{2+} channel is sufficient to mediate depolarization-induced exocytosis. J Neurochem 97:116–127
32. Faisal M, Ismail AA, Ibrahim AA, Bouzid H, Al-Sayari SA (2013) Highly efficient photocatalyst based on Ce doped ZnO nanorods: controllable synthesis and enhanced photocatalytic activity. Chem Eng J 229:225–233
33. Priya DS, Suriyaprabha R, Yuvakkumar R, Rajendran V (2014) Chitosan-incorporated different nanocomposite HPMC films for food preservation. J Nanopart Res 16:2248
34. Suriyaprabha R, Karunakaran G, Kavitha K, Yuvakkumar R, Rajendran V (2013) Application of silica nanoparticles in maize to enhance fungal resistance. IET Nanobiotechnol 8:133–137
35. Ramalingam KJ, Dhineshbabu NR, Srither SR, Saravanakumar B, Yuvakkumar R, Rajendran V (2014) Electrical measurement of PVA/graphene nanofibers for transparent electrode applications. Synth Met 191:113–119
36. Sankarrajan S, Aravindan S, Yuvakkumar R, Sakthipandi K, Rajendran V (2009) Anomalies of ultrasonic velocities, attenuation and elastic moduli in $Nd_{1-x}Sr_xMnO_3$ perovskite manganite materials. J Magn Magn Mater 321:3611–3620
37. Nathanael AJ, Yuvakkumar R, Hong SI, Oh TH (2014) Novel zirconium nitride and hydroxyapatite nanocomposite coating: detailed analysis and functional properties. ACS Appl Mater Interfaces 6: 9850–9857
38. Yuvakkumar R, Hong SI (2014) Green synthesis of spinel magnetite iron oxide nanoparticles. Adv Mater Res 1051:39–42
39. Suresh J, Yuvakkumar R, Sundrarajan M, Hong SI (2014) Green synthesis of magnesium oxide nanoparticles. Adv Mater Res 952: 141–144
40. Zuo J, Xu C, Liu X, Wang C, Wang C, Hu Y, Qian Y (1994) Study of the Raman spectrum of nanometer SnO_2. J Appl Phys 75:1835–1836.38
41. Dieguez A, Rodrıguez AR, Vila A, Morante JR (2001) The complete Raman spectrum of nanometric SnO_2 particles. J Appl Phys 9: 1550–1557
42. Kar A, Kundu S, Patra A (2011) Surface defect-related luminescence properties of SnO_2 nanorods and nanoparticles. J Phys Chem C 115:118–124
43. Yu B, Guo L, Yang Z, Zhu C, Gan F, Zhang G, Tang G, Wu X, Chen W (1999) The infrared vibration characteristics of SnO_2 nanoparticles. Phys Lett A 251:67–72
44. Sharma A, Tomar M, Gupta V (2012) Room temperature trace level detection of NO_2 gas using SnO_2 modified carbon nanotubes based sensor. J Mater Chem 22:23608–23616
45. Zhou JX, Zhang MS, Hong JM, Fang JL, Yin Z (2005) Structural and spectral properties of SnO_2 nanocrystal prepared by micro emulsion technique. Appl Phys A Mater Sci Process 81:177–182
46. Dutta K, De SK (2007) Optical and nonlinear electrical properties of SnO_2–polyaniline nanocomposites. Mater Lett 61:4967–4971
47. Saravanakumar B, Muthu Lakshmi S, Ravi G, Ganesh V, Sakunthala A, Yuvakkumar R (2017) Electrochemical properties of rice-like copper manganese oxide ($CuMn_2O_4$) nanoparticles for pseudocapacitor applications. J Alloys Compd 723:115–122
48. Gomez J, Kalu EE (2013) High-performance binder-free Co–Mn composite oxide supercapacitor electrode. J Power Sources 230: 218–224
49. Murugan R, Ravi G, Yuvakkumar R, Rajendran S, Maheswari N, Muralidharan G, Hayakawa Y (2017) Pure and Co doped CeO_2 nanostructure electrodes with enhanced electrochemical performance for energy storage applications. Ceram Int 43:10494–10501
50. Pusawale SN, Deshmukh PR, Lokhande CD (2011) Chemical synthesis of nanocrystalline SnO_2 thin films for supercapacitor application. Appl Surf Sci 257:9498–9502
51. Liu Y, Jiao Y, Zhang Z, Qu F, Umar A, Wu X (2014) Hierarchical SnO_2 nanostructures made of intermingled ultrathin nanosheets for environmental remediation, smart gas sensor, and supercapacitor applications. ACS Appl Mater Interfaces 6:2174–2184
52. Ai Hu Z, Long Xie Y, Xian Wang Y, Ping Mo L, Ying Yang Y, Yu Zhang Z (2009) Polyaniline/SnO_2 nanocomposite for supercapacitor applications. Mater Chem Phys 114:990–995
53. Meng X, Zhou M, Li X, Yao J, Liu F, He H, Xiao P, Zhang Y (2013) Synthesis of SnO_2 nanoflowers and electrochemical properties of Ni/SnO_2 nanoflowers in supercapacitor. Electrochim Acta 109:20–26
54. Sankar KV, Selvan RK (2015) The ternary $MnFe_2O_4$/graphene/polyaniline hybrid composite as negative electrode for supercapacitors. J Power Sources 275:399–407
55. Bashir B, Shaheen W, Asghar M, Warsi MF, Azhar Khan M, Haider S, Shakir I, Shahid M (2017) Copper doped manganese ferrites nanoparticles anchored on graphene nano-sheets for high performance energy storage applications. J Alloys Compd 695:881–887